Hydrometallurgy 208 (2022) 105810

Contents lists available at ScienceDirect

Hydrometallurgy

journal homepage: www.elsevier.com/locate/hydromet

Production of Mn_3O_4 nanoparticles from a manganiferous iron ore via reductive leaching, precipitation, and calcination

Mahmut Altiner [a], Soner Top [b], Chafia Bouchekrit [a,c], Sait Kursunoglu [b,*]

[a] *Cukurova University, Department of Mining Engineering, Division of Mineral Processing, Adana 01330, Turkey*
[b] *Abdullah Gul University, Department of Nanotechnology Engineering, Kayseri 38100, Turkey*
[c] *Ferhat Abbas University Setif 1, Optics and Precision Mechanics Institute, Emerging Materials Research Unit, 19000 Setif, Algeria*

ARTICLE INFO

Keywords:
Manganiferous iron ore
Mn_3O_4 nanoparticles
Reductive leaching
Precipitation
Calcination

ABSTRACT

The synthesis of Mn_3O_4 nanoparticles from a manganiferous iron ore through reductive leaching, precipitation, and calcination was investigated. The reductive leaching results showed that Mn (99.9%) was almost completely extracted into the leaching solution along with a substantial amount of Mg (99.9%), Al (99.5%), Ca (80%), and Fe (22.9%) under the following conditions: 30 g/L tartaric acid as a reducing agent, 1 M HCl solution, leaching temperature of 90 °C, and leaching duration of 3 h. In the first precipitation step, Fe and Al were expelled from the pregnant leach solution by the addition of NaOH prior to conducting the precipitation experiments for the production of manganese carbonate ($MnCO_3$) particles from the purified solution. In the second precipitation step, $MnCO_3$ particles were produced using sodium carbonate (Na_2CO_3) as the precipitating agent. The effects of parameters such as reaction temperature, Na_2CO_3 concentration, and experimental duration were investigated using the Taguchi approach. Manganse(II) was precipitated in the form of $MnCO_3$ particles (97.4%) under the following conditions: a temperature of 30 °C, Na_2CO_3 concentration of 0.014 mol/L, and duration of 30 min. The precipitate was observed to have a structure similar to that of rhodochrosite ($MnCO_3$). Thermogravimetric/differential thermal analyses were subsequently performed in three different atmospheres (air, oxygen, and nitrogen) to select a suitable atmosphere for calcination. The experimental results indicated the formation of hausmannite (Mn_3O_4) with a purity of 97.5% Mn_3O_4, 0.42% MgO, 1.66% CaO, and 0.34% FeO. The specific surface area, particle size, Curie temperature, magnetisation, coercivity, and remanence ratio of the final product obtained via 3 h of calcination at 350 °C were estimated to be 133.3 m^2/g, <142.2 nm, 56 K, 10.10 Am^2/kg, 0.35 T, and 0.19, respectively. The characterisation results revealed the excellent low-temperature ferromagnetic properties of the produced Mn_3O_4 nanoparticles.

1. Introduction

Manganese oxides have attracted attention for several decades owing to their extraordinary properties and applications in fields involving magnetic and electromagnetic materials (Zhang et al., 2010a), batteries, catalysts (Mansournia et al., 2015), and adsorbents (Shao et al., 2017). In particular, Mn_3O_4 is a highly significant manganese oxide that can be employed as an anode material with excellent electrochemical performance in rechargeable Li-CO_2 (Ma et al., 2018), Na-ion (Yusoff et al., 2020), and Li-ion (Meng et al., 2019) batteries, and supercapacitors (Liu et al., 2021). Its low cost, high specific capacitance, and environmentally friendly and non-poisonous nature showcase its tremendous potential as a leading supercapacitor electrode material for the future (Dubal and Holze, 2013). Furthermore, Mn_3O_4 can be used as a soft magnetic material (Song et al., 2013). However, Mn_3O_4 particles with high purity, nanostructure, and uniform particle size distribution must be produced for the aforementioned applications.

Several methods such as sol–gel synthesis, the facile gel route (Ullah et al., 2017), chemical deposition, the solvothermal process, the solvent-assisted hydrothermal method (Shaik et al., 2019), co-precipitation, precipitation conversion-roasting (Li et al., 2021), microwave- or ultrasonic-assisted production (Gopalakrishnan et al., 2005; Rohani Bastami and Entezari, 2012; Bastami and Entezari, 2012), and thermal decomposition (Gao et al., 2017) have recently been adopted for producing Mn_3O_4 particles with desirable properties using different resources such as $Mn(CH_3COO)_2$ (Song et al., 2013), $KMnO_4$, $MnSO_4$

---

* Corresponding author.
E-mail addresses: maltiner@cu.edu.tr (M. Altiner), soner.top@agu.edu.tr (S. Top), sait.kursunoglu@agu.edu.tr (S. Kursunoglu).

https://doi.org/10.1016/j.hydromet.2021.105810
Received 27 May 2021; Received in revised form 13 December 2021; Accepted 17 December 2021

Table 1
The conditions of leaching in the absence of reductant.

Solid-to-liquid ratio	Acid concentration, M	Temperature, °C	Time, h	Stirring speed, rpm
1/10, 1/15, 1/20	1	70	1	300

Table 2
Experimental parameters designed according to the Taguchi approach to produce $MnCO_3$ [L9 (3^3)].

Exp. no	Temperature (°C)	Amount of Na_2CO_3 added (mol/L)	Time (min.)
E1	30	0.014	30
E2	30	0.018	120
E3	30	0.022	210
E4	75	0.014	120
E5	75	0.018	210
E6	75	0.022	30
E7	95	0.014	210
E8	95	0.018	30
E9	95	0.022	120

Table 3
The chemical composition of the ore sample.

Element	Fe	Mn	Al	Ca	Mg	P	S	LOI[a]
% (w/w)	25.0	15.0	1.54	3.29	0.94	0.18	0.11	10.9

[a] Loss on ignition.

(Zhang et al., 2010a; Zhang et al., 2013), $MnCl_2{\cdot}4H_2O$ (Ahmed et al., 2010), $MnCO_3$ (Gao et al., 2017; Lei et al., 2006), $MnSiO_3$ (Li et al., 2019), manganese(II) glycerolate (Jankovský et al., 2015), and manganese ore (Zawrah et al., 2020). Manganese oxide particles have also been recovered from waste batteries (Mylarappa et al., 2016).

Mylarappa et al. (Zawrah et al., 2020) indicated that manganese ore could be leached in a nitric acid solution at 90 °C for 24 h using glucose as a reducing agent to realise enhanced selective dissolution of Mn with a high leaching efficiency. Subsequently, Mn_3O_4 was precipitated from the pregnant leach solution under certain conditions by the addition of ammonia or sodium hydroxide. Sinha and Purcell (2019) examined the reduction chemistry and leaching mechanism of manganese oxides from Mn-based ores by analysing the effect of reducing agents with potential for the leaching of Mn with high recoveries. Various inorganic chemicals, such as sulfur dioxide (Sun et al., 2013); ferrous sulfate (Das et al., 1982), iron powder (Bafghi et al., 2008), and other iron salts (Kholmogorov et al., 2000); H_2O_2 (El Hazek et al., 2006); and organic reductants, such as lactic acid (Ma et al., 2015), formic acid (Lu et al., 2015), oxalic acid (Sahoo et al., 2001), potassium oxalate (Freitas et al., 2013), malonic acid (Lasheen et al., 2014), citric acid (Godunov et al., 2012), glucose (Furlani et al., 2006), sucrose (Wang et al., 2017), lactose (De Michelis et al., 2009), and agricultural waste or biomass (Hariprasad

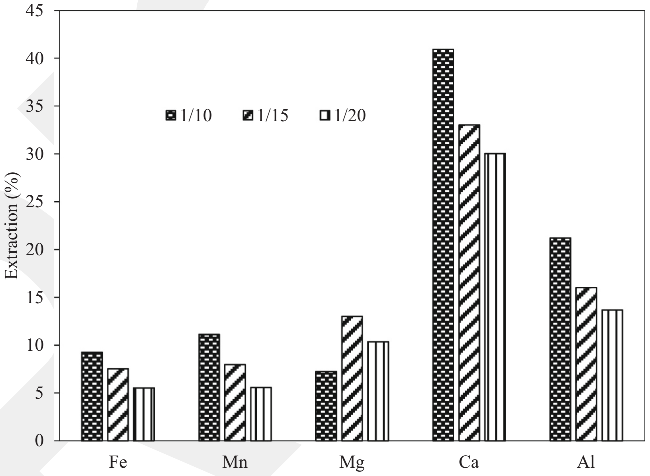

Fig. 2. The effect of solid-to-liquid ratio on leaching (other leaching conditions: 70 °C, 1 h duration, 300 rpm, 1 M HCl).

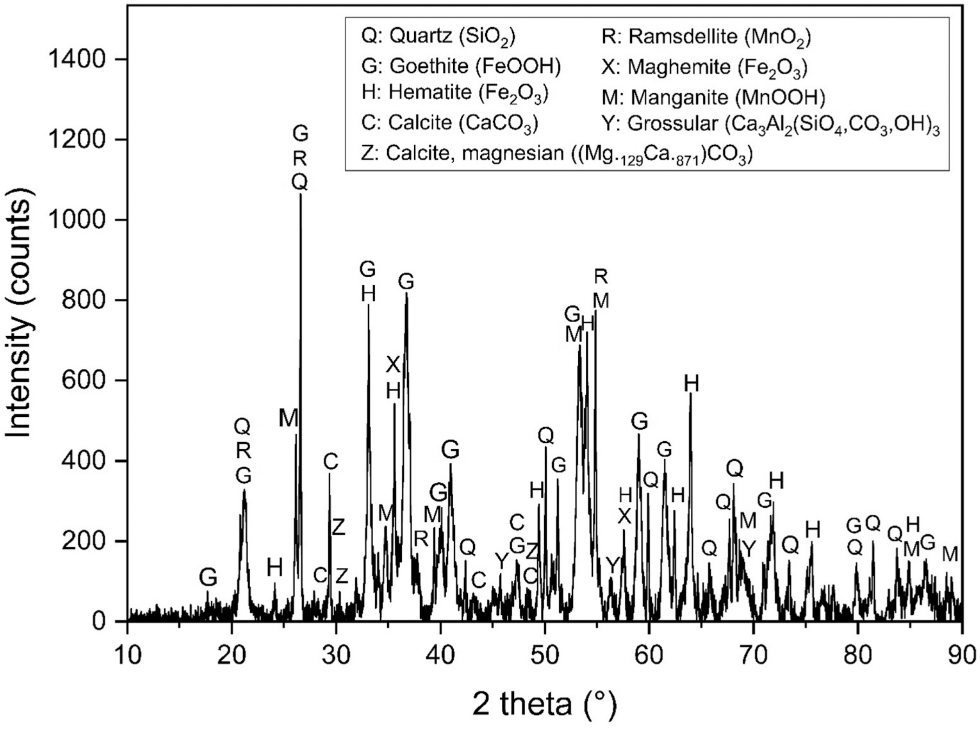

Fig. 1. The XRD pattern of the ore.

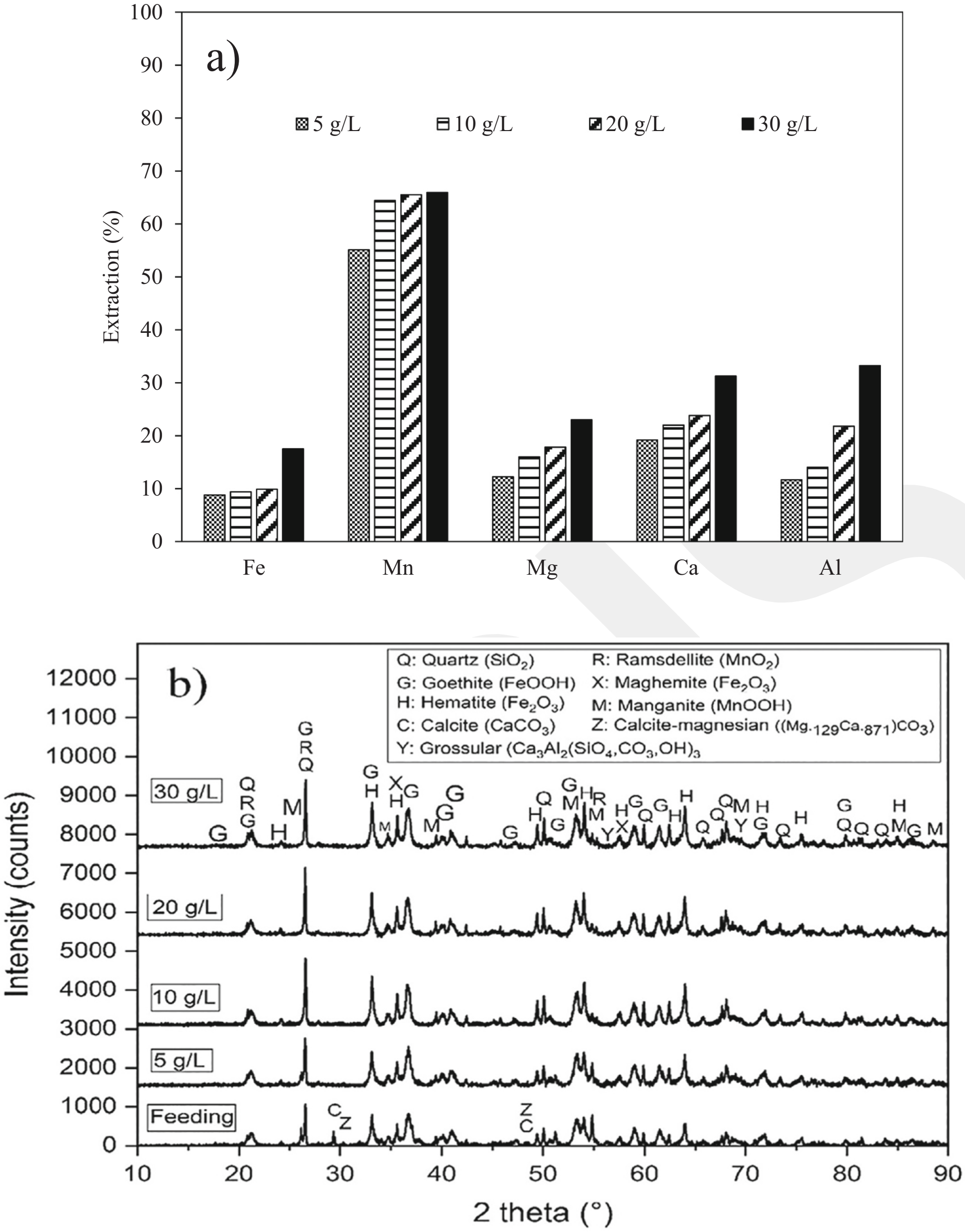

Fig. 3. The effect of tartaric acid on leaching: a) extraction values b) XRD patterns of the residues (other leaching conditions: 1/10 solid-to-liquid ratio, 70 °C, 1 h duration, 300 rpm, 1 M HCl).

Table 4
Manganese extraction orders utilizing various amounts of organic acids.

Order	Organic, 5 g/L	Mn extraction, %	Organic, 30 g/L	Mn extraction, %
1	Tartaric acid	55.1	Oxalic acid	76.6
2	Citric acid	54.7	Tartaric acid	65.9
3	Glucose	44.6	Citric acid	64.8
4	Maleic acid	43.1	Glucose	61.5
5	Oxalic acid	38.7	Maleic acid	54.7
6	Sucrose	32.7	Sucrose	54.6
7	Acetic acid	5.74	Acetic acid	11.9

Other leaching conditions: 1/10 solid-to-liquid ratio, 70 °C, 1 h duration, 300 rpm, 1 M HCl.

et al., 2007; Lasheen et al., 2009; Cheng et al., 2009; Xiong et al., 2018), have also been employed to dissolve Mn from ores to obtain high recoveries.

Various separation-based methods involving carbonate (Lin et al., 2016), hydroxide (Ristić et al., 2013), and oxidative (Oruê et al., 2020) precipitation have been extensively adopted to selectively recover Mn from leachates. Lin et al. (2016) evaluated the aforementioned approaches and elucidated the separation mechanism of Mn from leachate containing Ca and Mg impurities. The precipitation behaviour of metals in hydroxide or carbonate form were noted to be different. An increase in the solution pH from 2 to 13 was found to linearly increase the precipitation of Mn, Ca, and Mg, whereas the precipitation rates of Mn, Ca, and Mg in carbonate form showed solution-pH-dependent differences. Subsequently, selective separation of Mn(II) from a pregnant leach solution (PLS) containing Ca and Mg impurities was realised using a carbonate chemical (Na_2CO_3 or NH_4HCO_3) (Lin et al., 2016; Ali et al., 2020). Li et al. (2021) indicated that the amount of alkali used in the

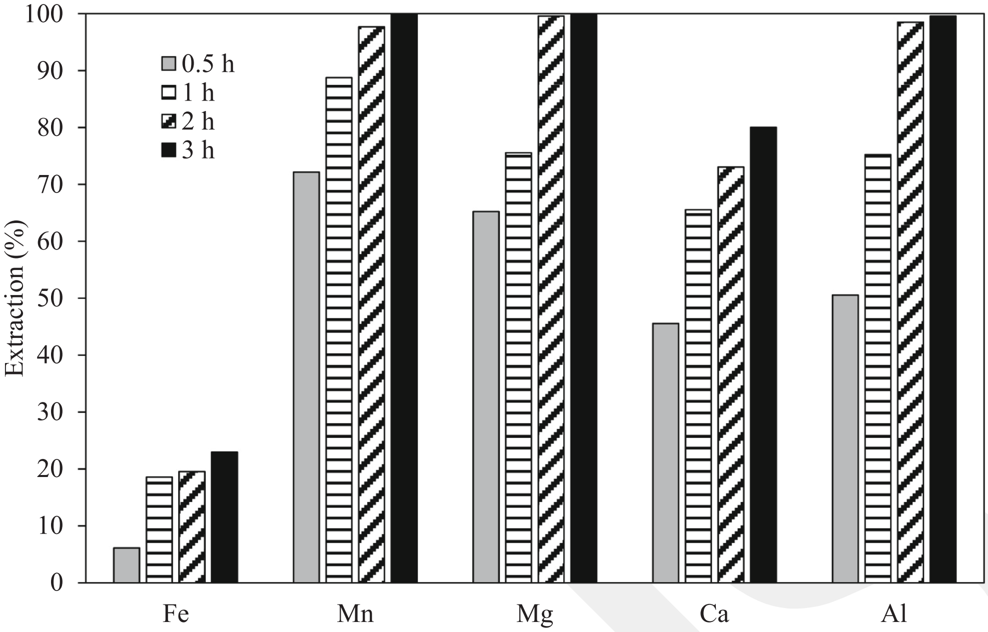

Fig. 4. The leaching behaviour of Fe, Mn, Mg, Ca, and Al from ore as a function of leaching time (other leaching conditions: 1/10 solid-to-liquid ratio, 300 rpm, 30 g/L tartaric acid, 90 °C, and 1 M HCl).

Table 5
Changes in metal ion concentrations before and after the addition of sodium hydroxide.

Elements	Concentration, mg/L	
	Before NaOH addition	After NaOH addition
Mn	11,949	11,729
Fe	4800	43
Mg	975	766
Ca	2400	1886
Al	1113	26

Table 6
Experimental results of the precipitation tests.

Exp. no	Mn precipitation (%)	Mg precipitation (%)	Ca precipitation (%)	pH (±0.1)
E1	97.4	9.65	7.80	7.11
E2	99.8	20.5	14.9	8.73
E3	99.9	43.0	41.3	9.27
E4	96.6	13.6	88.2	7.89
E5	99.7	75.4	96.4	8.27
E6	100.0	92.7	98.3	9.08
E7	95.5	56.1	63.6	7.90
E8	99.7	97.7	99.1	8.65
E9	100.0	95.4	92.1	9.13

precipitation stage for producing Mn hydroxide considerably influenced the morphology and particle size of the final product. Particles of Mn_3O_4 with an irregular cubic shape were consequently produced with an alkali-to-manganese mole ratio of 1.6 after calcination. An increase in this ratio to 4.0 yielded Mn_3O_4 particles with a cubic structure and uniform particle size distribution.

The aforementioned literature review suggests that the recovery of Mn from a PLS in carbonate form is more convenient and efficient than that in hydroxide form. The primary objectives of the present study were to investigate (i) the production of Mn_3O_4 nanoparticles with extraordinary properties from a manganiferous iron ore using tartaric acid as a reducing agent in a solution of HCl, (ii) the NaOH-induced removal of impurities from the solution produced after reductive leaching, (iii) the sodium-carbonate-assisted precipitation from a purified Mn(II) bearing liquor, and (iv) the calcination of the precipitate. The reductive leaching of Mn in an HCl solution was initially investigated in the presence of various reducing agents. To the best of our knowledge, this is the first report on the use of tartaric acid as a reducing agent in an HCl solution for the extraction of Mn from a manganiferous iron ore. In the first step of the precipitation tests, Fe and Al impurities were removed from the PLS using sodium hydroxide. Additional precipitation tests based on the Taguchi approach were conducted using sodium carbonate as a precipitating agent to obtain high-purity $MnCO_3$ from the PLS of low iron and aluminium content. Finally, the precipitated product was converted into Mn_3O_4 by calcination under certain conditions that significantly influenced the properties of the product. The calcined product was characterised by X-ray diffraction (XRD), X-ray fluorescence (XRF), scanning electron microscopy (SEM), particle size distribution (PSD), Brunauer–Emmett–Teller (BET), and magnetic hysteresis (M–H curve) analyses.

2. Materials and method

2.1. Materials

The ore sample was generously provided by the Sonmez Cement Company in Ceyhan-Adana, Turkey. The chemical composition of the ore was determined by XRF (Panalytical MiniPal 4) and atomic absorption spectrometry (AAS; Perkin Elmer PinAAcle 900H). The sulfur and phosphorous contents in the ore were determined using Eltra CS 580 and Nanocolor 100 D spectrophotometers. The XRD analysis was performed using a Bruker D8 Discover setup equipped with a Lynxeye detector to determine the mineralogical compositions of the samples. The XRD data were acquired over 15 min in the range of 10°–90° with a step size of 0.02°. The percentage estimation and mineral identification were performed using DIFFRAC.SUITE EVA software with an up-to-date PDF 2 database. Prior to conducting the reductive leaching experiments, the ore was crushed using a laboratory-type jaw crusher and subsequently ground in a ball mill to reduce its particle size below 100 μm.

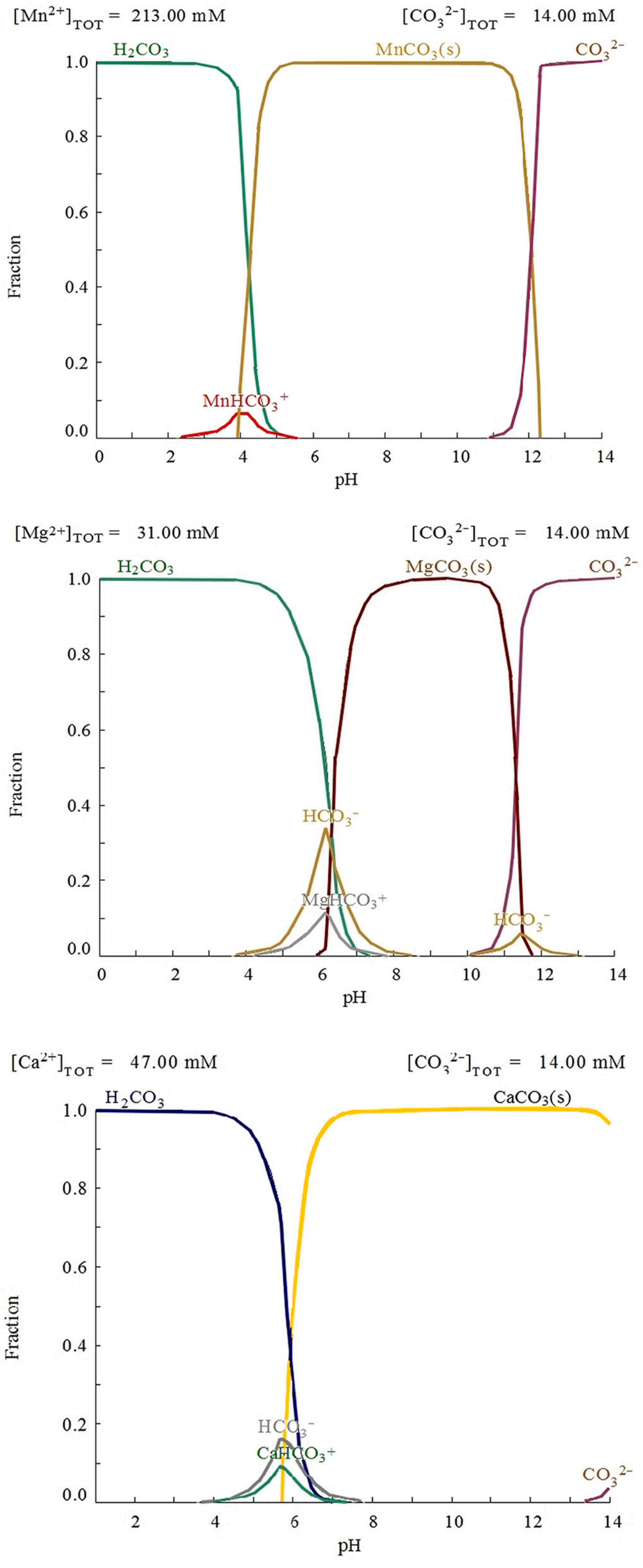

Fig. 5. The precipitation of manganese as $MnCO_3$ ($[Mn^{2+}]$: 213 mM, $[Mg^{2+}]$: 31 mM, $[Ca^{2+}]$: 47 mM, Na_2CO_3: 14 mM) (Medusa Software).

2.2. Method

2.2.1. Reductive leaching tests

The effects of different organic acids, such as tartaric acid ($C_4H_6O_6$, Carlo Erba), oxalic acid ($C_2H_2O_4$, Merck), citric acid ($C_6H_8O_7$, Merck), glucose ($C_6H_{12}O_6$, Merck), sucrose ($C_{12}H_{22}O_{11}$, Isolab), maleic acid ($C_4H_4O_4$, Aromel Chemistry), and acetic acid (CH_3COOH, Merck), in HCl (Merck) solution were examined for the selective extraction of Mn from the investigated ore. The reductive leaching tests were performed in a 250 mL beaker reactor equipped with a circulating water bath and a glass condenser attached to minimise evaporation. A magnetic stirrer (MTOPS, Ms300 Hs) was used to agitate the slurry at a stirring speed of 300 rpm. The slurries obtained upon completion of the reductive leaching tests were filtered with Whatman 1 filter paper, and the residues were washed with deionised water. The collected solutions were measured and analysed by AAS. The effects of solid-to-liquid ratio on the reductant-free extraction of Fe, Mn, Mg, Ca, and Al from the ore were investigated. The conditions of the leaching tests in the absence of reductant are summarized in Table 1.

2.2.2. Precipitation tests

Precipitation experiments were conducted on the clarified leach liquors i.e. pregnant leach solutions (PLSs) collected from the reductive leaching experiments under the determined optimal conditions. A typical precipitation experiment was performed at ambient temperature using 75 mL of the solution in a glass beaker heated on a temperature-controlled hot plate equipped with a magnetic stirrer. The glass beaker was covered with Al foil during the experiment to avoid excessive evaporation. Upon reaching the desired temperature, the precipitating agent was slowly delivered using a syringe, while the solution was stirred at a speed of 250 rpm. The impurities in the solution (Fe and Al) were precipitated in hydroxide form by the addition of NaOH, resulting in an increase in the solution pH that was monitored using a pH meter (WTW 3110). The slurry obtained after the precipitation experiment was filtered, and the precipitate was washed with deionised water. The collected solutions were measured and analysed by AAS.

The solution with negligible contents of Fe and Al was subsequently subjected to additional precipitation tests to obtain high-purity $MnCO_3$. The effects of temperature, amount of Na_2CO_3, and reaction time on the production of $MnCO_3$ from the purified solution were investigated using the Taguchi approach. The obtained experimental results were converted into three categories of signal-to-noise (S/N) ratios: (i) larger-to-better, (ii) smaller-to-better, and (iii) nominal-to-better. The larger-to-better ratio was selected for the precipitation of Mn, whereas the smaller-to-better ratio was selected as the output parameter for the precipitation of Mg and Ca. Furthermore, the contribution of each parameter to the precipitation test was calculated. The three independent variables with three levels are presented in Table 2. Statistical analysis was conducted using MINITAB 17.0 software. Based on the results obtained in this step, $MnCO_3$ particles were prepared under optimal conditions for use in the calcination tests.

2.2.3. Calcination tests

The thermal behaviour of the product obtained in the precipitation stage was first investigated using a thermogravimetric (TG) analyser from 25 °C to 1000 °C at a heating rate of 20 °C/min under (i) air, (ii) nitrogen, and (iii) oxygen. Subsequently, calcination experiments were conducted in a temperature range of 350–850 °C in a muffle furnace for different durations under the optimal atmosphere. The effects of the calcination time (Ti) and temperature (Te) on the properties of the obtained products were investigated. The experimental conditions for calcination were denoted as TiX-TeX. For example, Ti3-Te350 refers to an experiment performed at 350 °C for 3 h.

2.2.4. Characterisation

The phase properties of the obtained products were determined by XRD. The surface morphologies of the selected products were imaged by SEM (FEI Quanta 650). The chemical compositions of the investigated products were determined by AAS and XRF. The specific surface areas (SSAs) of the products of interest were measured using the BET method, and the PSDs were determined using a Malvern Nano-ZS apparatus. The

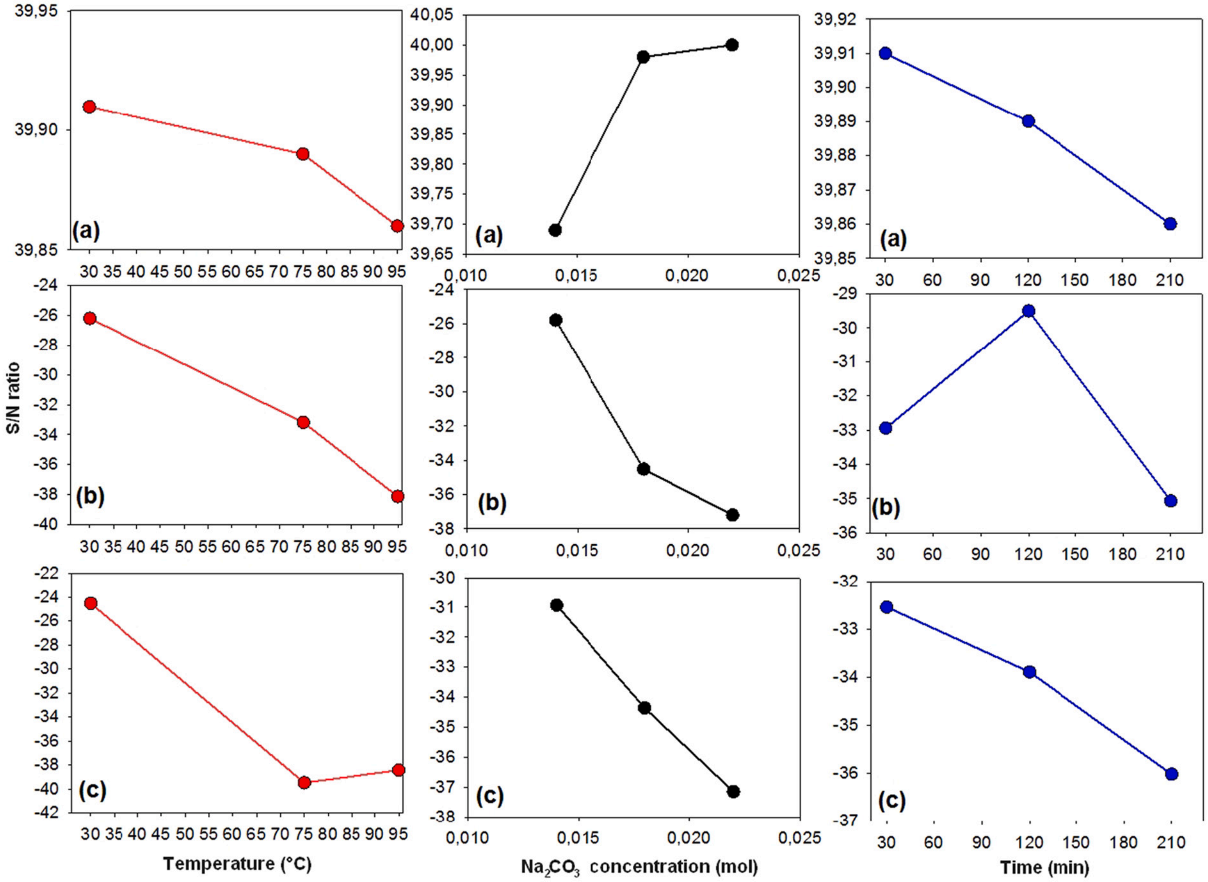

Fig. 6. The S/N values for the production of $MnCO_3$: (a) Manganese precipitation, (b) Magnesium precipitation and (c) Calcium precipitation.

Table 7
Variance analysis (ANOVA).

Source	DF	Adj SS	Adv MS	F-value	*p*-Value	Contribution ratio (%)
Manganese precipitation						
Temperature	2	0.5883	0.2941	1.12	0.471	2.39
*Na$_2$CO$_3$	2	22.8274	11.4137	43.59	0.022	92.77
Time	2	0.6668	0.3334	1.27	0.440	2.70
Error	2	0.5236	0.2618			2.14
Total	8	24.6061				
Magnesium precipitation						
*Temperature	2	5263.1	2631.53	45.66	0.021	50.67
*Na$_2$CO$_3$	2	4161.0	2080.52	36.10	0.027	40.05
Time	2	848.3	424.17	7.36	0.120	8.17
Error	2	115.3	57.63			1.11
Total	8	10,387.7				
Calcium precipitation						
*Temperature	2	9461.7	4730.83	20.69	0.046	87.19
Na$_2$CO$_3$	2	915.8	457.91	2.00	0.333	8.43
Time	2	17.0	8.50	0.04	0.964	0.16
Error	2	457.3	228.63			4.21
Total	8	10,851.7				100.00

The R^2 value for the precipitation of manganese, magnesium and calcium as carbonate form was found to be 97.87%, 98.89% and 95.79%, respectively. These values indicate that the models used in this study are valid. In addition, "*" indicates the most effective parameter in the precipitation tests.

magnetic hysteresis properties of the selected products were examined at 5 K and 300 K in a magnetic field of up to ±3 T using a physical property measurement system (Quantum Design, PPMS Dynacool-9). Additionally, zero-field-cooling (ZFC) and field-cooling (FC) procedures were performed at a magnetic field of 0.01 T to determine the Curie temperature (T_C) of the final product.

3. Results and discussion

The chemical compositions of the ore are listed in Table 3. Fig. 1 shows the XRD patterns of the ore samples. Quantitative phase analysis was conducted based on the values of the reference intensity ratio (RIR). As shown in Fig. 1, the ore sample consisted of hematite (Fe_2O_3; 16.3%), goethite (FeO(OH); 16.1%), manganite (MnO(OH); 14.8%), maghemite-C (Fe_2O_3; 12.7%), calcium silicate ($Ca_3Al_2(SiO_4, CO_3, OH)$; 12.5%), quartz ($SiO_2$; 9.2%), calcite ($CaCO_3$; 8.3%), ramsdellite ($MnO_2$; 7.8%), and calcite-magnesian ($Mn_{.129}Ca_{.871}(CO_3)$); 2.2%) mineral phases.

3.1. Effects of solid-to-liquid ratio on extraction

Fig. 2 shows the extraction percentages of the aforementioned metals. The highest extraction of Mn (11.1%) was achieved at a solid-to-liquid ratio of 1/10, whereas 9.23% Fe, 7.24% Mg, 40.9% Ca, and 21.2% Al were drawn into the leaching solution. Increasing the solid-to-liquid ratio resulted in a decrease in the extraction of each metal. For example, the extraction of Mn decreased linearly from 11.1% to 5.58% as the solid-to-liquid ratio decreased from 1/10 to 1/20. This is due to the decrease in H^+ ions required per gram of the sample during leaching. The reduction reaction of MnO_2 in acidic solutions is shown in (Eq. (1)). In addition, the other metals exhibited similar extraction behaviour, except for Mg, which exhibited a negligible decrease. Consequently, the solid-to-liquid ratio was fixed at 1/10 in the subsequent experiments.

$$MnO_2 + 4H^+ + 2e^- = Mn^{2+} + 2H_2O, \Delta G^\circ_{343} = -230.022 \text{ kJ} \qquad (1)$$

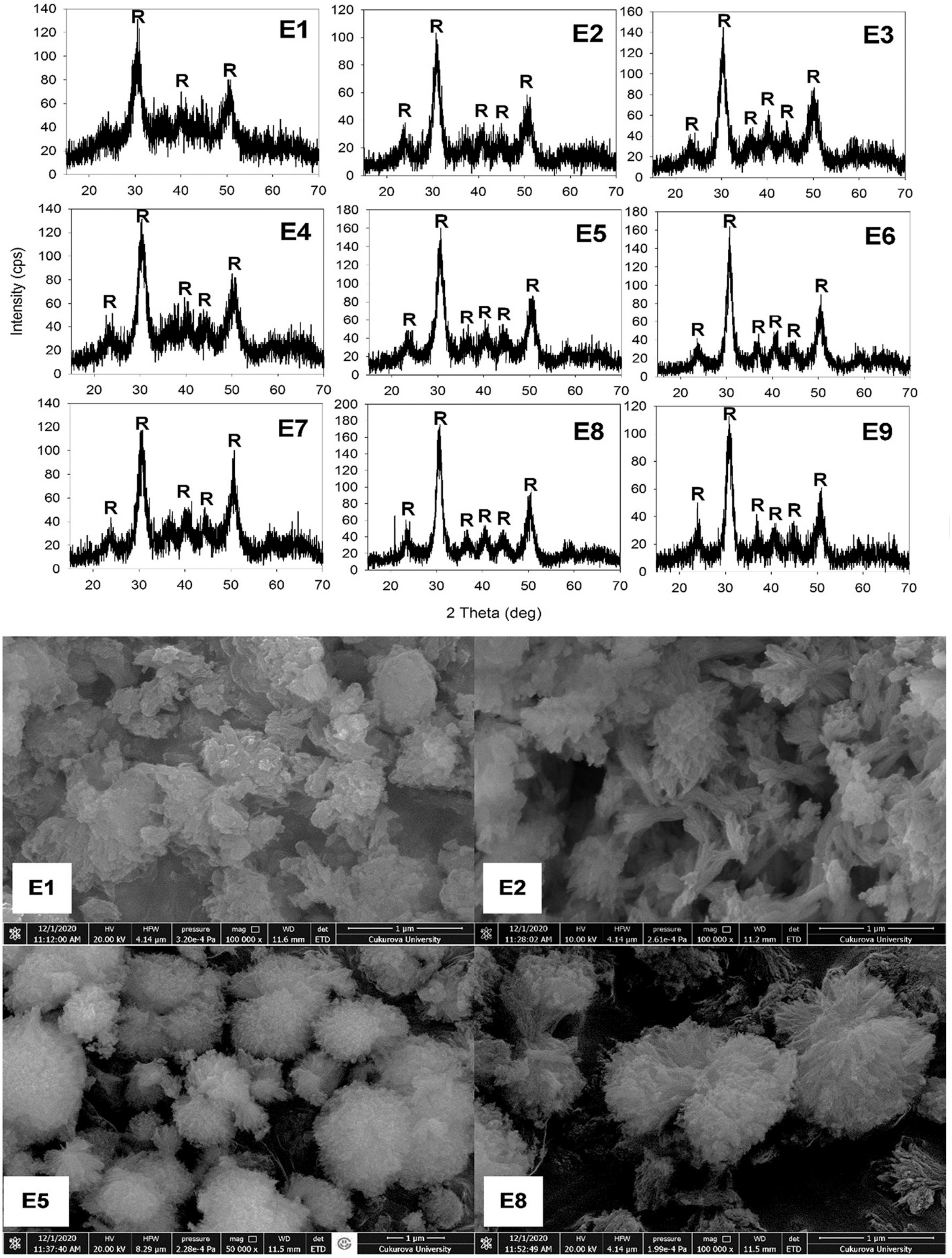

Fig. 7. The XRD patterns of rhodochrosite (R, $MnCO_3$, PDF Card No: 00-044-1472) mineral in the precipitation tests and some SEM images of the selected rhodochrosite mineral.

3.2. *Effects of acid concentration and temperature on extraction*

The extraction of Fe, Mn, Mg, Ca, and Al was found to increase with increasing leaching temperature and HCl concentration (Fig. S1). The XRD analysis of the residues revealed the disappearance of Mn-related minerals with increasing leaching temperature and HCl concentration (Fig. S2). Moreover, the peaks corresponding to the quartz content in the residue increased in intensity owing to its resistance to leach in HCl. The leaching efficiency of the metals was strongly influenced by the temperature and acid concentration. Because these experiments were aimed at the selective extraction of Mn from an ore, the reductive leaching tests were conducted under the following optimised parameters: a leaching time of 1 h, stirring speed of 300 rpm, temperature of 70 °C, and HCl concentration of 1 M, with the ore being leached at an efficiency of

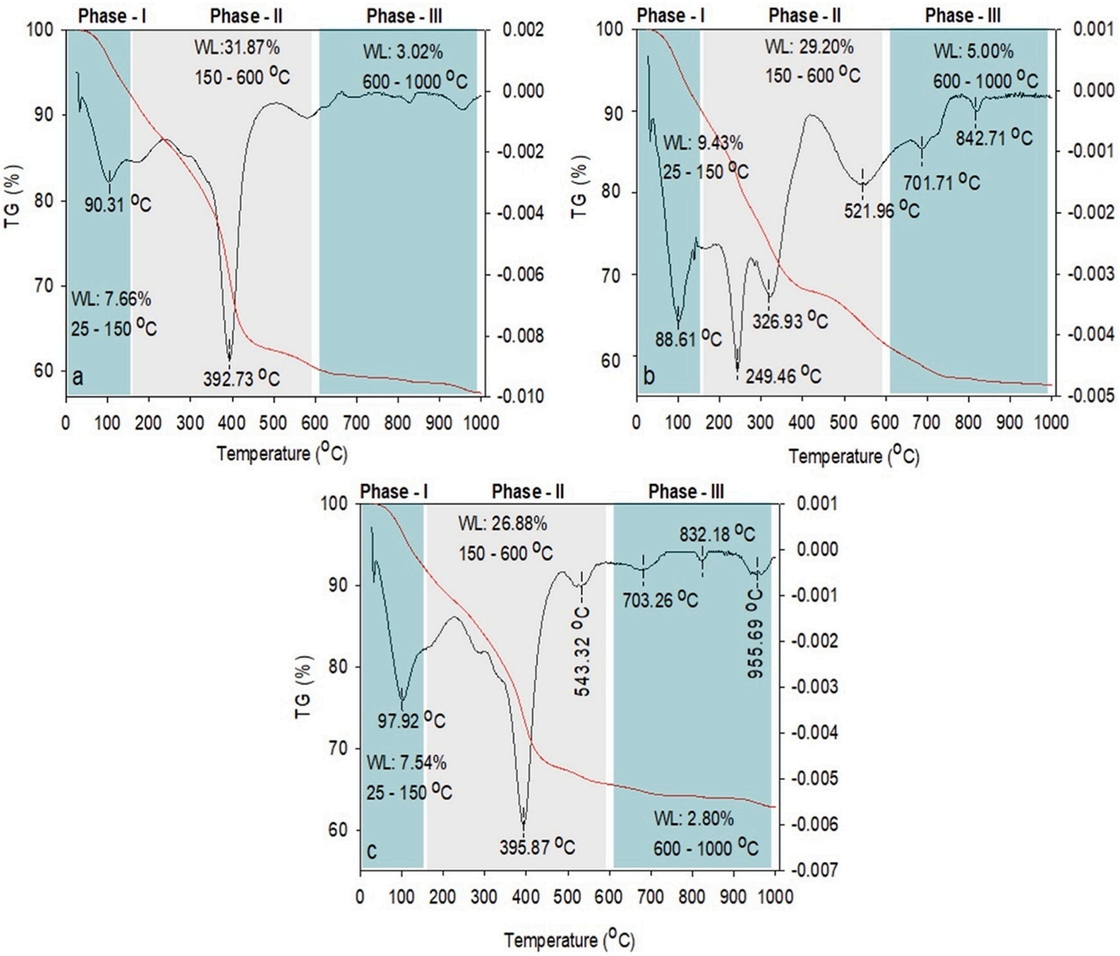

Fig. 8. The thermal behaviour of rhodochrosite ($MnCO_3$) produced at the E2 condition at a temperature of 25–1000 °C in the presence of (a) nitrogen, (b) oxygen, and (c) air atmosphere (WL = weight loss).

Table 8
Determination of mineral phases under various calcination conditions.

Calcination conditions[a]	Mineral(*s*)[b]	PDF card no
Ti3-Te350	Hausmannite (Mn_3O_4)	01-075-1650
Ti5-Te350	Hausmannite (Mn_3O_4)	01-074-6605
Ti3-Te600	γ-Mn_3O_4	00-018-0803
	$Mn_{2.03}O_4$	01-073-5018
Ti5-Te600	γ-Mn_3O_4	00-018-0803
	β-Mn_3O_4	01-076-2337
Ti3-Te850	β-Mn_3O_4	01-086-2337
Ti5-Te850	β-Mn_3O_4	01-086-2337

[a] Roasting time Ti = 3 or 5 h, temperature Te = 350, 600 or 850 °C.
[b] Refer to Fig. S5.

11.0% Mn and 9.52% Fe.

3.3. *Effects of reductants on extraction*

The effects of reductants on the extraction of Fe, Mn, Mg, Ca, and Al from the ore were investigated. The use of reductants resulted in enhanced extraction of the concerned metals (Fig. 3a and Fig. S3). The extraction of Mn was estimated as 76.6%, 64.8%, 65.9%, 54.4%, 61.5%, 54.6%, and 11.9% in the presence of oxalic acid, citric acid, tartaric acid, maleic acid, glucose, sucrose, and acetic acid at concentrations of 30 g/L, respectively. In contrast, the extraction of Fe reduced by 23% in the presence of each reductant. The extraction of metals from the ore in decreasing order was as follows: Mn > Ca > Al > Mg > Fe. Furthermore, the amount of the reducing agent used in the leaching tests significantly influenced the leaching behaviour of these metals. For example, the extraction of Mn in the range 5.74%–55.1% with the descending order given in Table 4 at 5 g/L reducing agents increased to the range 11.9%–76.6% at a higher dosage of 10 g/L reducing agent, but with a different descending order (Table 4).

The XRD analysis indicated that the characteristic peaks of the manganite and ramsdellite minerals started to decrease in intensity or disappear, confirming the extraction of Mn from the ore (Fig. 3b and Fig. S4). However, Mn-bearing minerals were detected in the residue obtained via acetic-acid-assisted leaching, because of the considerably low extraction of Mn. The decrease in the peak intensities of Mn-bearing minerals clearly led to an increase in the intensity of the quartz peaks. These experiments indicated that Mn could be leached with an efficiency greater than 60% using oxalic acid, tartaric acid, citric acid, or glucose as a reducing agent. Therefore, the selective leaching of Mn from a manganiferous iron ore using tartaric acid as a reducing agent in an HCl solution was targeted; this has not been previously reported. In addition, the synthesis of Mn_3O_4 nanoparticles from the produced reductive leaching solution has not been previously described. The chemical reaction for the selective extraction of Mn using tartaric acid as a reducing agent in an HCl solution can be expressed as follows (Eq. (2)):

$$5MnO_2 + 10H^+ + C_4H_6O_6 = 4CO_2 + 5Mn^{2+} + 8H_2O, \Delta G^\circ_{343} = -1295.545\ \text{kJ} \tag{2}$$

The process of leaching was conducted at a higher temperature using 30 g/L tartaric acid as a reductant to realise enhanced Mn extraction.

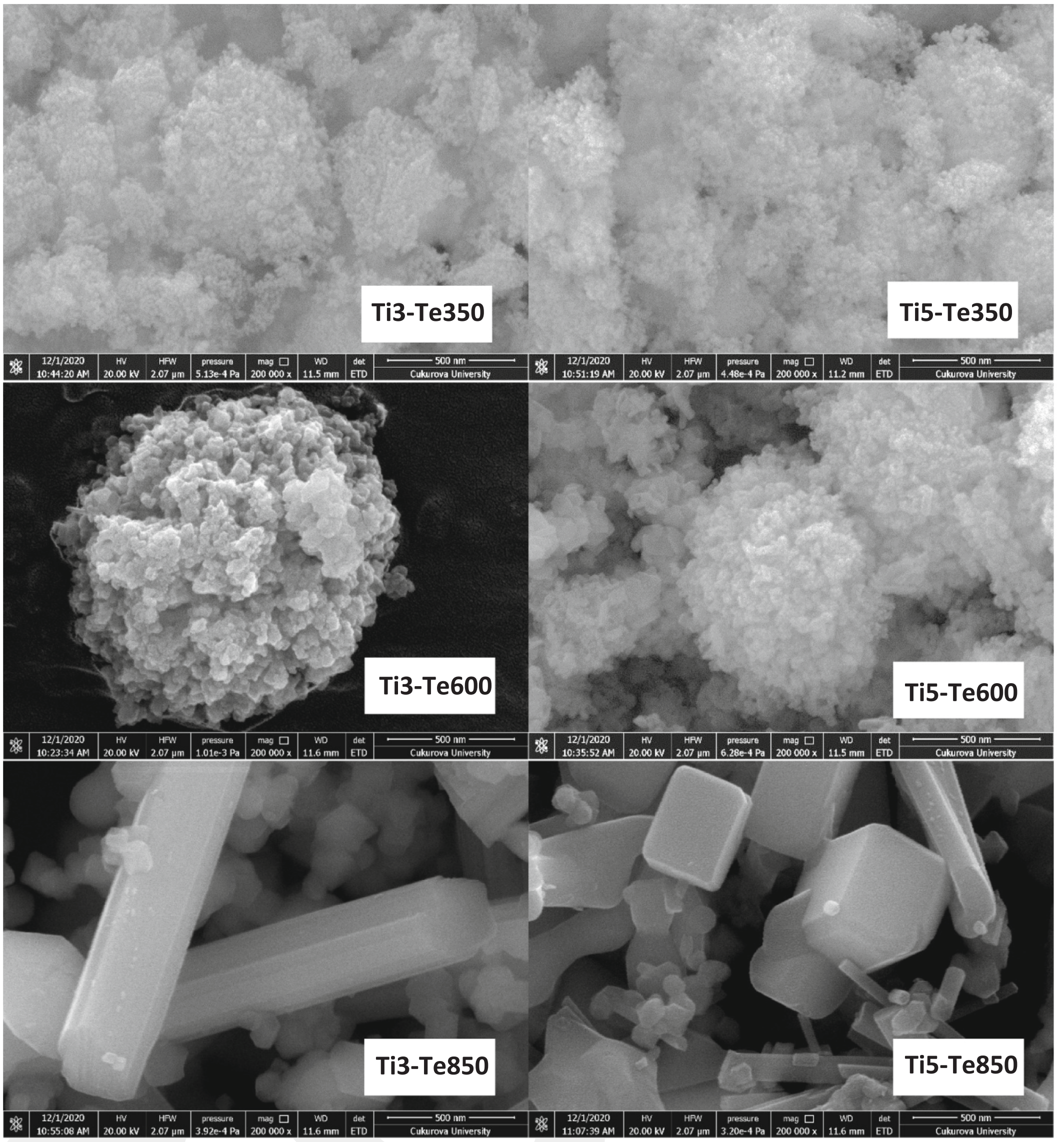

Fig. 9. The SEM images of the produced Mn-oxide nanoparticles after the calcination process (codes explained in Table 8).

Tests conducted at 90 °C for 3 h resulted in 99.9% Mn being drawn into the leaching solution along with Mg (99.9%), Al (99.5%), Ca (80%), and Fe (22.9%) as shown in Fig. 4.

3.4. *Precipitation of manganese carbonate ($MnCO_3$)*

The stock solution for the precipitation study was collected under the following conditions: a solid-to-liquid ratio of 1/10, stirring speed of 300 rpm, temperature of 90 °C, duration of 3 h, HCl concentration of 1 M, and tartaric acid concentration of 30 g/L. The solution pH was increased up to 5 (±0.1) from −1.6 by the addition of 0.065 mol of NaOH to remove impurities. The concentrations of impurities (Fe, Mg, Ca, and Al) in the purified solution decreased in the first step. The Mn concentration slightly decreased from the leach liquor presumably because of the adsorption of Mn ions on the fine particles (Table 5).

The precipitation temperature, amount of Na_2CO_3, and precipitation time were investigated using the Taguchi approach for producing high-purity $MnCO_3$ in the second-step precipitation tests; similar studies have been previously conducted (Ali et al., 2020; Zhang et al., 2010b). The precipitation percentages of each element and the final pH values of the solutions are listed in Table 6.

The final pH of the solution varied between 7.11 and 9.27, which is consistent with the precipitation diagram of $MnCO_3$ particles constructed with respect to the solution pH. Fig. 5 demonstrates that $MnCO_3$ can be produced in a pH range of 7–11, theoretically validating the experimental findings of this study. Furthermore, the following chemical reaction (Eq. (3)) occurred spontaneously at 30 °C:

$$MnCl_2 + Na_2CO_3 = MnCO_3 + 2NaCl, \Delta G^{\circ}_{303} = -139.962 \text{ kJ} \tag{3}$$

Accordingly, Mn precipitated as $MnCO_3$; however, Mg and Ca did not precipitate with high precipitation percentages under the employed conditions. For example, the precipitation percentages of Mn were in the ranges of 97.4%–99.9%, 96.6%–100%, and 95.5%–100% at temperatures of 30, 75, and 95 °C, respectively. These results suggested that the reaction temperature did not affect the precipitation of Mn, and that specific conditions were required to precipitate Ca and Mg in carbonate form. Based on the precipitation conditions, the precipitation percentages of Mg and Ca varied in the 9.65%–97.7% and 7.80%–99.1% ranges, respectively. The results from this study indicated that Mn could be precipitated along with the Mg and Ca impurities with an increase in the reaction temperature and amount of Na_2CO_3. The experimental results were converted into S/N values, as shown in Fig. 6.

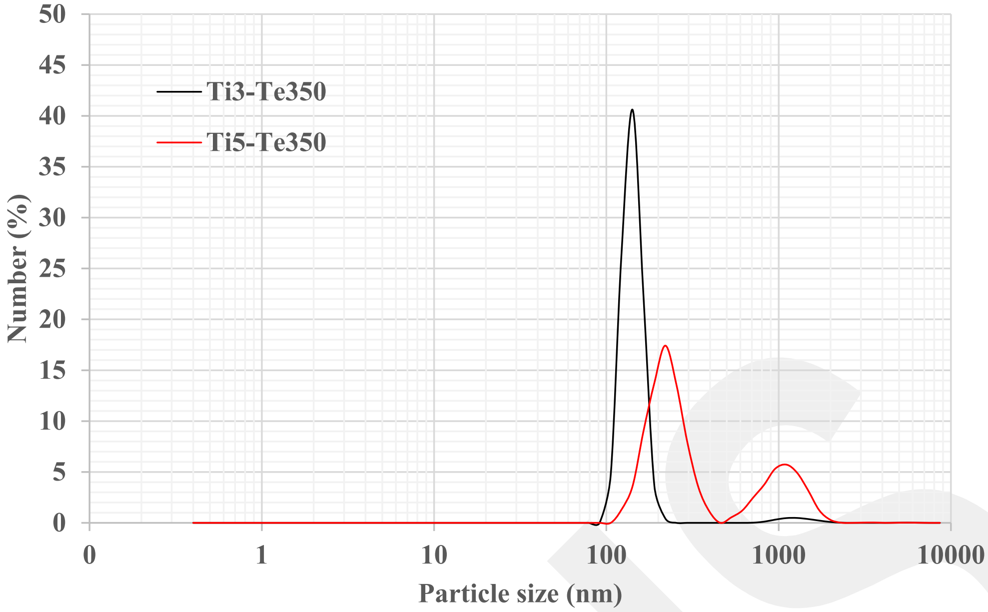

Fig. 10. The particle size distributions of the samples produced under Ti3-Te350 and Ti5-Te350 conditions.

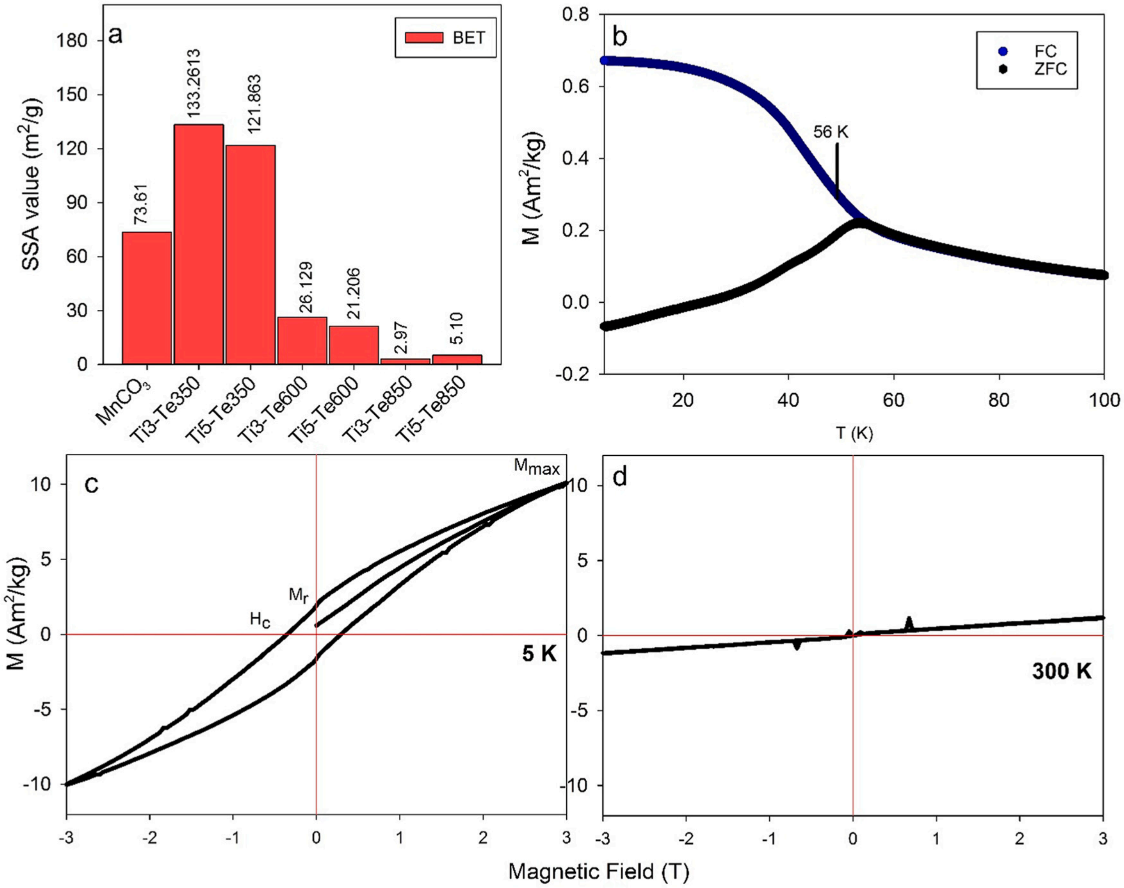

Fig. 11. (a) The SSA value of the products, (b) The magnetic behaviour of the product in field-cooling and zero-field-cooling modes, (c) The M-H hysteresis curves of the product produced under the Ti3-Te350 condition at a temperature of 5 K, (d) The M-H hysteresis curves of the product formed under the Ti3-Te350 condition at a temperature of 300 K.

The influence of precipitation conditions can be conveniently evaluated using these graphs. The effects of the conditions on the precipitation percentage of Mn were in the following order: amount of Na_2CO_3 > reaction time > reaction temperature. ANOVA analysis (Table 7) indicated that the amount of added Na_2CO_3, with a contribution ratio of 92.77%, was the only effective parameter among these factors; the experimental error was estimated to be 2.14%.

Although the reaction temperature did not considerably influence the precipitation of Mn, an increase in the reaction temperature resulted in the precipitation of Mg and Ca, which lowered the purity of $MnCO_3$. These findings were confirmed by chemical analysis of the concerned products. For example, the product was primarily composed of 46.4% Mn, 0.17% Mg, 0.79% Ca, 0.17% Fe, and 42.3% LOI when the precipitation test was performed under the following conditions (E1): a temperature of 30 °C, Na_2CO_3 concentration of 0.014 mol/L, and duration of 30 min. The purity of the product obtained under the E8 set of conditions was low because of the precipitation of Ca and Mg along with Mn in carbonate form, which contained 35.9% Mn, 1.83% Mg, 7.41% Ca, 0.13 Fe%, and 43.8% LOI.

The polymorphs and phase properties of the products were characterised by XRD and SEM analyses (Fig. 7). The peaks were consistent with the pattern of the rhodochrosite mineral ($MnCO_3$, PDF Card No: 00–044-1472). Although the precipitation percentages of Ca and Mg were higher, no peaks of Ca or Mg carbonate minerals were observed owing to the detection limit of XRD (Ali et al., 2020). In addition, the XRD analysis indicated that the product was amorphous and poorly crystallised, which is consistent with the SEM images of the products obtained under the E1, E2, E5, and E9 conditions. The obtained $MnCO_3$ products were not smooth and well-shaped. Therefore, based on the characterisation test results, the product synthesised under the E1 set of conditions was adopted for subsequent calcination tests.

3.5. *Production and characterisation of hausmannite (Mn_3O_4)*

Several reactions may occur during the process of decomposition, depending on the atmosphere. The $MnCO_3$ particles are decomposed into Mn oxide and CO_2 gas; however, different forms of these Mn oxide particles (MnO, Mn_2O_3, Mn_3O_4, Mn_5O_8, and MnO_2) could be generated (Biernacki and Pokrzywnicki, 1999). The calcination atmosphere is known to play a key role in the oxidation properties of Mn oxides (Jankovský et al., 2015; Augustin et al., 2015). For example, MnO particles can be produced in the presence of Ar, whereas Mn_2O_3 can be produced via decomposition of $MnCO_3$ particles in air (Pinc et al., 2016).

The production of Mn oxide particles must be carefully conducted, because the calcination temperature and atmosphere significantly affect their properties such as particle size, surface area, and Mn oxidation state. Therefore, the decomposition behaviour of the products in a temperature range of 25–1000 °C were evaluated under (i) nitrogen, (ii) oxygen, and (iii) air. The TG/differential thermal analysis (DTA) curves of the product produced under E1 are shown in Fig. 8.

The TG curves were divided into three phases (phase I [25–150 °C], phase II [150–600 °C], and phase III [600–1000 °C]), based on the endothermic peaks observed in each DT curve, to elucidate the decomposition mechanism of the products. Moreover, the DT curves were used as an indicator to determine the temperature-dependent phase transformations of the calcined products. As shown in the phase I region, a peak representing the evaporation of molecular water appeared in a temperature zone of 85.07–97.94 °C. A weight loss (WL) of 7.66% was achieved by the E1 product under a nitrogen atmosphere.

The endothermic peaks determined in the phase 2 region (150–600 °C) validated the temperature-dependent decomposition of $MnCO_3$ and the release of CO_2 gases. The decomposition temperature of $MnCO_3$ was noted to be approximately 395 °C. The highest WL of the product (31.9%) was obtained in this region (Fig. 8a), which was in line with the theoretical value (31.3%) corresponding to the decomposition of $MnCO_3$ into Mn_2O_3 nanoparticles. These reactions can be represented as follows (Eq. (4)) (Pourmortazavi et al., 2012; Wang et al., 2013a):

$$MnCO_3 + MnO_2 = Mn_2O_3 + CO_2, \Delta G^{\circ}_{623} = -51.177 \text{ kJ} \tag{4}$$

Fig. 8b shows several endothermic peaks in the phase 1 and 2 regions with respect to a pure oxygen atmosphere. These peaks are presumably due to the temperature-dependent oxidation tendencies of the obtained Mn oxide products. The following chemical reactions presumably represent the formation of various Mn oxide compounds (Eqs. (5)–(8)):

$$2MnCO_3 + O_2 = 2MnO_2 + 2CO_2, \Delta G^{\circ}_{623} = -139.795 \text{ kJ} \tag{5}$$

$$2Mn_2O_3 + O_2 = 4MnO_2, \Delta G^{\circ}_{623} = -37.441 \text{ kJ} \tag{6}$$

$$4MnCO_3 + O_2 = 2Mn_2O_3 + 4CO_2, \Delta G^{\circ}_{623} = -242.149 \text{ kJ} \tag{7}$$

$$6MnCO_3 + O_2 = 2Mn_3O_4 + 6CO2, \Delta G^{\circ}_{623} = -312.833 \text{ kJ} \tag{8}$$

The mass loss of the product in air was estimated to be 26.9% (phase 2; Fig. 8c), validating the decomposition of $MnCO_3$ into Mn_3O_4 (theoretical value: 28%). The DT curves revealed that the thermal behaviour of the product in nitrogen and air atmospheres were similar; thus, the decomposition process could be conveniently controlled to produce Mn oxide particles with desirable properties. However, the presence of several endothermic peaks in Fig. 8b hints at issues that could affect this production. Therefore, the effects of calcination parameters on the properties of the product in an air atmosphere were investigated.

The effects of the calcination conditions on the phase properties of each product were probed by XRD analysis, summarized in Table 8. The rhodochrosite mineral was converted into hausmannite under the Ti3-Te350 conditions. However, two peaks corresponding to Mn_3O_4 were observed. Increasing the reaction time to 5 h at the same temperature (Ti5-Te350) led to the appearance of additional peaks representing hausmannite in the XRD pattern. The hausmannite mineral was well crystallised with extended reaction times. A mixture of Mn oxide minerals was obtained under the Ti3-Te600 conditions. Two major Mn oxide minerals were determined to be γ-Mn_3O_4 and $Mn_{2.03}O_4$. Increasing the calcination time at the same temperature (Ti5-Te600) resulted in the disappearance and appearance of the $Mn_{2.03}O_4$ and β-Mn_3O_4 peaks, respectively. These findings are consistent with those of a previous study (He et al., 2003). The phase change of Mn oxide minerals from Mn_2O_3/$Mn_{2.03}O_4$ to Mn_3O_4 occurred with increasing temperature (Liu et al., 2014; Narayani et al., 2019). Peaks representing β-Mn_3O_4 were obtained under the Ti3-Te850 conditions. As mentioned earlier, Mn oxide minerals with well-crystallised properties can be produced via prolonged calcination. The β-Mn_3O_4 mineral was obtained under the Ti5-Te850 conditions. These findings were confirmed by the SEM images shown in Fig. 9.

The products obtained at 350 °C were neither well crystallised nor amorphous (Ti3-Te350 and Ti5-Te350); however, an increase in the calcination temperature to 600 °C led to the formation of well-shaped and flow-like structures (Ti3-Te600 and Ti5-Te600). Moreover, rod-like and cubic crystals were observed in the SEM images of β-Mn_3O_4 produced under the Ti3-Te850 and Ti5-Te850 conditions, respectively. The calcination temperature played a crucial role in the preparation of Mn oxide nanoparticles with different structural properties.

Fig. 10 shows the particle size distribution of the products obtained at 350 °C. The product formed within 3 h exhibited a unimodal distribution (Ti3-Te350). Particle size analysis revealed that 97.9% of the product synthesised under the Ti3-Te350 conditions was smaller than 142.2 nm. However, increasing the duration led to an increase in particle size and yielded a bimodal distribution (Ti5-Te350). After 5 h, the PSD showed that 65.3% of the product (Ti5-Te350) was smaller than 209.8 nm.

Fig. 11a shows that Mn oxides with various specific surface area (SSA) values can be produced depending on the experimental conditions. Prior to the calcination, the SSA of the $MnCO_3$ particles was estimated to be 73.61 m^2/g. After calcination, the SSA values of Mn oxide products were in the range of 2.97–133.3 m^2/g, which is consistent with those obtained in previous studies (Dubal and Holze, 2013; Gao et al., 2017; Zhang et al., 2013; Aghazadeh et al., 2017; Pudukudy et al., 2014; Li et al., 2016). The electrical capacities of Mn_3O_4 nanoparticles are known to increase with increasing SSA. A larger surface area enables faster access of electrolytes and ions to the active material.

Therefore, Mn_3O_4 with a high SSA must be prepared for use in Li-ion batteries (Meng et al., 2019; Wang et al., 2013b). The SSA of the product increased from 73.61 m^2/g to 133.26 m^2/g owing to the decomposition of $MnCO_3$ into Mn oxide nanoparticles at high temperatures. This finding is consistent with those of a previous study (Liu et al., 2019), in which Mn_3O_4 nanoparticles with a SSA of 90 m^2/g were produced from $MnCO_3$ particles with a SSA of 15 m^2/g after 6 h of calcination at 300 °C. An increase in the calcination time resulted in a decrease in the SSA of the product, leading to the synthesis of a product with a SSA of 121.9 m^2/g under the Ti5-Te350 conditions (Fig. 11). A dramatic decrease in SSA was observed with an increase in the calcination temperature and time. Products with SSA values of 26.12 m^2/g and 21.20 m^2/g were obtained under the Ti3-Te600 and Ti5-Te600 conditions, respectively. Furthermore, products with SSA values of 2.97 m^2/g and 5.10 m^2/g were synthesised under the Ti3-Te850 and Ti5-Te850 conditions, respectively.

The magnetic behaviour of Mn_3O_4 is known to be strongly dependent on the ambient temperature. Consequently, Mn_3O_4 nanoparticles exhibit ferromagnetic behaviour at low temperatures (<100 K), and display paramagnetic behaviour under ambient conditions. The Curie temperature (T_C), which can be used to monitor the ferromagnetic-to-paramagnetic conversion behaviour of the product, is known to be 42 K for Mn_3O_4 nanoparticles (Dwight and Menyuk, 1960; Chang et al., 2004; Azzoni et al., 2001). Two different experiments (zero-field-cooling and field-cooling) were performed to determine the Curie temperature of the product synthesised in this study. As shown in Fig. 11b, the magnetisation reached a maximum and subsequently started to decrease at a temperature of 56 K, which was determined to be the T_C of the product. Furthermore, this finding is in good agreement with that of a previous study (Vazquez-Olmos et al., 2005); however, the T_C value is lower than those obtained in other previous studies (Gopalakrishnan et al., 2005; Bastami and Entezari, 2012; Dwight and Menyuk, 1960; Chang et al., 2004; Azzoni et al., 2001). The value of T_C is known to be significantly influenced by the production conditions of the materials; for example, a mixture of Mn_3O_4 and polyethylene glycol (PEG) (80:20) exhibits paramagnetic and ferromagnetic behaviour at temperatures >50 K and <50 K, respectively (Durmus et al., 2011).

Magnetic hysteresis (M–H) curves of the product obtained under the Ti3-Te350 conditions were collected at temperatures of 5 K and 300 K under a magnetic field of ±3 T (Fig. 11c and d). The M–H curves corresponding to the zero-field-cooling and field-cooling experiments of the product at 5 K revealed its ferromagnetic behaviour; moreover, the magnetisation value (M_{max}) of the product was estimated to be 10.10 Am^2/kg, which is considerably low compared to that of bulk Mn_3O_4 (Ms: 38 Am^2/kg) (Tebble and Craik, 1969). The maximum saturation magnetisation of bulk Mn_3O_4 could not be attained. Similar results have been obtained in a previous study (Rani et al., 2018) because of the misaligned spin configurations of nanosized materials, which resulted in a low magnetic moment of the product (Jahromi et al., 2015; Selvan et al., 2008; Sherin et al., 2014). The remanence ratio (M_r/M_{max}) was estimated to be 0.19 using data from the M–H curve. The coercivity (H_c) of the product (0.35 T) was smaller compared to previously reported values of H_c [15, 71], indicating that the smaller H_c is possibly related to the properties of the crystals (nanorods and nanoparticles) in the product. A decrease in the particle size increases the coercivity of the product (Song et al., 2013). The M–H curve is linear at 300 K, indicating that the product exhibited paramagnetic behaviour (M_{max}: 0.20 Am^2/kg); therefore, no coercivity was observed. This finding is in line with that of a previous study (Bastami and Entezari, 2012). Chemical analysis indicated that a high-purity product with a composition of 97.5% Mn_3O_4, 0.42% MgO, 1.66% CaO, and 0.34% FeO can be produced. The purity of this product is significantly higher than that of a product obtained in a previous study in which iron-oxide-rich Mn_3O_4 was obtained from a low-grade manganese ore (Zawrah et al., 2020).

4. Conclusions

The production of high-purity Mn_3O_4 nanoparticles from a manganiferous iron ore by hydro- and pyro-metallurgical methods, including reductive leaching, precipitation, and calcination, was investigated. The experimental results of the reductive leaching tests revealed the possibility of dissolving Mn with a high extraction percentage (99.9%) from the ore using tartaric acid as a reducing agent in an HCl solution. Iron and aluminium impurities in the leachate were initially removed by the addition of NaOH. In the second step of the precipitation tests, the effects of precipitation conditions on the production of $MnCO_3$ from the purified solution were investigated using the Taguchi approach, which showed that the contribution ratios of the parameters could be ordered as follows: amount of Na_2CO_3 > reaction time > reaction temperature. However, increasing the amount of Na_2CO_3 triggered the precipitation of Ca and Mg in carbonate form, resulting in a decrease in the purity of the $MnCO_3$ product. Rhodochrosite particles ($MnCO_3$; 97.4%) were precipitated under the following conditions: a temperature of 30 °C, Na_2CO_3 concentration of 0.014 mol/L, and a duration of 30 min. Calcination was conducted at different temperatures, durations, and atmospheres. The polymorphs and crystal properties of the Mn_3O_4 product changed with respect to the duration and temperature of calcination. The product obtained under the Ti3-Ti350 conditions was determined to be Mn_3O_4 with extraordinary properties such as a high SSA (132.55 m^2/g), particle size of <142.2 nm, remarkable low-temperature ferromagnetic behaviour (5 K), and high chemical purity (97.5% Mn_3O_4, 0.42% MgO, 1.66% CaO, and 0.34% FeO).

Declaration of Competing Interest

The authors declare that they have no known competing financial interests or personal relationships that could have appeared to influence the work reported in this paper.

Acknowledgments

The study was financially supported by The Scientific and Technological Research Council of Turkey [TÜBİTAK Project ID: 119M690] and Cukurova University [Project ID: FBA-2020-13057]. The authors thank the editors and anonymous reviewers for improving the manuscript.

Appendix A. Supplementary data

Supplementary data to this article can be found online at https://doi.org/10.1016/j.hydromet.2021.105810.

References

Aghazadeh, M., Asadi, M., Ganjali, M.R., Norouzi, P., Sabour, B., Emamalizadeh, M., 2017. Template-free preparation of vertically-aligned Mn 3 O 4 nanorods as high supercapacitive performance electrode material. Thin Solid Films 634, 24–32.

Ahmed, K.A.M., Zeng, Q., Wu, K., Huang, K., 2010. Mn3O4 nanoplates and nanoparticles: synthesis, characterization, electrochemical and catalytic properties. J. Solid State Chem. 183, 744–751.

Ali, S., Iqbal, Y., Shah, K.H., Fahad, M., 2020. Synthesis and kinetic modeling of manganese carbonate precipitated from manganese sulfate solution. Chem. Eng. Commun. 1–12.

Augustin, M., Fenske, D., Bardenhagen, I., Westphal, A., Knipper, M., Plaggenborg, T., Kolny-Olesiak, J., Parisi, J., 2015. Manganese oxide phases and morphologies: a study on calcination temperature and atmospheric dependence. Beilstein J. Nanotechnol. 6, 47–59.

Azzoni, C.B., Mozzati, M.C., Malavasi, L., Ghigna, P., Flor, G., 2001. Magnetic and X-ray diffraction investigation on Mg1− xMn2+ xO4 spinels. Solid State Commun. 119, 591–595.

Bafghi, M.S., Zakeri, A., Ghasemi, Z., Adeli, M., 2008. Reductive dissolution of manganese ore in sulfuric acid in the presence of iron metal. Hydrometallurgy 90, 207–212.

Bastami, T.R., Entezari, M.H., 2012. Synthesis of manganese oxide nanocrystal by ultrasonic bath: effect of external magnetic field. Ultrason. Sonochem. 19, 830–840.

Biernacki, L., Pokrzywnicki, S., 1999. The Thermal Decomposition of Manganese Carbonate Thermogravimetry and Exoemission of Electrons, 55, pp. 227–232.

Chang, Y., Xu, X., Luo, X., Chen, C., Yu, D., 2004. Synthesis and characterization of Mn3O4 nanoparticles. J. Cryst. Growth 264, 232–236.

Cheng, Z., Zhu, G., Zhao, Y., 2009. Study in reduction-roast leaching manganese from low-grade manganese dioxide ores using cornstalk as reductant. Hydrometallurgy 96, 176–179.

Das, S., Sahoo, P., Rao, P., 1982. Extraction of manganese from low-grade manganese ores by FeSO4 leaching. Hydrometallurgy 8, 35–47.

De Michelis, I., Ferella, F., Beolchini, F., Olivieri, A., Vegliò, F., 2009. Characterisation and classification of solid wastes coming from reductive acid leaching of low-grade manganiferous ore. J. Hazard. Mater. 162, 1285–1291.

Dubal, D.P., Holze, R., 2013. Self-assembly of stacked layers of Mn3O4 nanosheets using a scalable chemical strategy for enhanced, flexible, electrochemical energy storage. J. Power Sources 238, 274–282.

Durmus, Z., Tomaş, M., Baykal, A., Kavas, H., Toprak, M.S., 2011. PEG-assisted Synthesis of Mn3O4 Nanoparticles: A Structural and Magnetic Study, Synthesis and Reactivity in Inorganic, Metal-organic, and Nano-metal Chemistry, 41, pp. 768–773.

Dwight, K., Menyuk, N., 1960. Magnetic properties of Mn 3 O 4 and the canted spin problem. Phys. Rev. 119, 1470.

El Hazek, M., Lasheen, T., Helal, A., 2006. Reductive leaching of manganese from low grade Sinai ore in HCl using H2O2 as reductant. Hydrometallurgy 84, 187–191.

Freitas, R.M., Perilli, T.A., Ladeira, A.C.Q., 2013. Oxidative precipitation of manganese from acid mine drainage by potassium permanganate. J. Chem. 2013.

Furlani, G., Pagnanelli, F., Toro, L., 2006. Reductive acid leaching of manganese dioxide with glucose: identification of oxidation derivatives of glucose. Hydrometallurgy 81, 234–240.

Gao, Y., Zheng, D., Xu, X., Lou, J., Wang, J., 2017. Facile synthesis of porous cube-like MnO 2 microstructures and their supercapacitive properties. Mater. Lett. 204, 161–164.

Godunov, E., Artamonova, I., Gorichev, I., Lainer, Y.A., 2012. Interaction of manganese (IV) oxide with aqueous solutions of citric and sulfuric acids. Russian Metal. 2012, 39–44.

Gopalakrishnan, I.K., Bagkar, N., Ganguly, R., Kulshreshtha, S.K., 2005. Synthesis of superparamagnetic Mn3O4 nanocrystallites by ultrasonic irradiation. J. Cryst. Growth 280, 436–441.

Hariprasad, D., Dash, B., Ghosh, M., Anand, S., 2007. Leaching of manganese ores using sawdust as a reductant. Miner. Eng. 20, 1293–1295.

He, W., Zhang, Y., Zhang, X., Wang, H., Yan, H., 2003. Low Temperature Preparation of Nanocrystalline Mn2O3 Via Ethanol-thermal Reduction of MnO2, 252, pp. 285–288.

Jahromi, S.P., Pandikumar, A., Goh, B.T., Lim, Y.S., Basirun, W.J., Lim, H.N., Huang, N. M., 2015. Influence of particle size on performance of a nickel oxide nanoparticle-based supercapacitor. RSC Adv. 5, 14010–14019.

Jankovský, O., Sedmidubský, D., Šimek, P., Sofer, Z., Ulbrich, P., Bartůněk, V., 2015. Synthesis of MnO, Mn2O3 and Mn3O4 nanocrystal clusters by thermal decomposition of manganese glycerolate. Ceram. Int. 41, 595–601.

Kholmogorov, A., Zhyzhaev, A., Kononov, U., Moiseeva, G., Pashkov, G., 2000. The production of manganese dioxide from manganese ores of some deposits of the Siberian region of Russia. Hydrometallurgy 56, 1–11.

Lasheen, T., El Hazek, M., Helal, A., 2009. Kinetics of reductive leaching of manganese oxide ore with molasses in nitric acid solution. Hydrometallurgy 98, 314–317.

Lasheen, T., Abu Elenein, S., Saleh, W., Orabi, A., Ismaiel, D., 2014. Reductive leaching kinetics of low grade manganese deposits in H2SO4 solution using malonic acid as reducing agent. Int. J. Sci. 15, 151–163.

Lei, S., Tang, K., Fang, Z., Liu, Q., Zheng, H., 2006. Preparation of α-Mn2O3 and MnO from thermal decomposition of MnCO3 and control of morphology. Mater. Lett. 60, 53–56.

Li, F., Wangyang, P., Zada, A., Humayun, M., Wang, B., Qu, Y., 2016. Synthesis of hierarchical Mn 2 O 3 microspheres for photocatalytic hydrogen production. Mater. Res. Bull. 84, 99–104.

Li, B., Zhang, X., Dou, J., Hu, C., 2019. Facile synthesis of pseudocapacitive Mn3O4 nanoparticles for high-performance supercapacitor. Ceram. Int. 45, 16297–16304.

Li, Y., Li, Y., Zhang, Z., He, X., Chen, J., 2021. Preparation of Mn3O4 by precipitation conversion-roasting method and its morphological evolution. Ceram. Int. 47 (15), 21570–21575. https://doi.org/10.1016/j.ceramint.2021.04.168.

Lin, Q.-q., Gu, G.-h., Wang, H., Wang, C.-q., Liu, Y.-c., Zhu, R.-f., Fu, J.-g., 2016. Separation of manganese from calcium and magnesium in sulfate solutions via carbonate precipitation. Trans. Nonferrous Metals Soc. China 26, 1118–1125.

Liu, M., Wang, Y., Cheng, Z., Zhang, M., Hu, M., Li, J., 2014. Electrospun Mn2O3 nanowrinkles and Mn3O4 nanorods: morphology and catalytic application. Appl. Surf. Sci. 313, 360–367.

Liu, Y., Zhang, P., Zhan, J., Liu, L., 2019. Heat treatment of MnCO3: an easy way to obtain efficient and stable MnO2 for humid O3 decomposition. Appl. Surf. Sci. 463, 374–385.

Liu, X., Zhong, M., Fu, Z., Xu, X., Wang, C., Yuan, L., Tang, Y., 2021. From hierarchically porous carbon to Mn3O4/carbon composites for high voltage aqueous supercapacitors. J. Power Sources 485, 229111.

Lu, Y., Ma, H., Huang, R., Yuan, A., Huang, Z., Zhou, Z., 2015. Reductive leaching of low-grade pyrolusite with formic acid. Metall. Mater. Trans. B 46, 1709–1715.

Ma, H., Lu, Y., Chen, D., Ming, X., Li, W., Yuan, A., Wei, D., Wei, S., 2015. Reductive leaching of low grade pyrolusite ore with lactic acid. Chin. J. Process. Eng. 15, 976–981.

Ma, W., Lu, S., Lei, X., Liu, X., Ding, Y., 2018. Porous Mn2O3 cathode for highly durable Li–CO2 batteries. J. Mater. Chem. A 6, 20829–20835.

Mansournia, M., Azizi, F., Rakhshan, N., 2015. A novel ammonia-assisted method for the direct synthesis of Mn3O4 nanoparticles at room temperature and their catalytic activity during the rapid degradation of azo dyes. J. Phys. Chem. Solids 80, 91–97.

Meng, S., Yan, W., Ma, X., Sun, D., Jin, Y., He, K., 2019. Hierarchical structured Mn2O3 nanomaterials with excellent electrochemical properties for lithium ion batteries. RSC Adv. 9, 1284–1289.

Mylarappa, M., Lakshmi, V.V., Mahesh, K.R.V., Nagaswarupa, H.P., Raghavendra, N., 2016. A facile hydrothermal recovery of nano sealed MnO2particle from waste batteries: an advanced material for electrochemical and environmental applications. In: IOP Conference Series: Materials Science and Engineering, 149.

Narayani, L., Angadi, V.J., Sukhdev, A., Challa, M., Matteppanavar, S., Deepthi, P., Kumar, P.M., Pasha, M., 2019. Mechanism of high temperature induced phase transformation and magnetic properties of Mn3O4 crystallites. J. Magn. Magn. Mater. 476, 268–273.

Oruê, B.P., Botelho Junior, A.B., Tenório, J.A.S., Espinosa, D.C.R., Baltazar, M.D.P.G., 2020. Kinetic study of manganese precipitation of nickel laterite leach based-solution by ozone oxidation. Ozone Sci. Eng. 1–15.

Pinc, J., Jankovský, O., Bartůněk, V., 2016. Preparation of manganese oxide nanoparticles by thermal decomposition of nanostructured manganese carbonate. Chem. Pap. 71, 1031–1035.

Pourmortazavi, S.M., Rahimi-Nasrabadi, M., Davoudi-Dehaghani, A.A., Javidan, A., Zahedi, M.M., Hajimirsadeghi, S.S., 2012. Statistical optimization of experimental parameters for synthesis of manganese carbonate and manganese oxide nanoparticles. Mater. Res. Bull. 47, 1045–1050.

Pudukudy, M., Yaakob, Z., Rajendran, R., 2014. Facile synthesis of mesoporous α-Mn 2 O 3 microspheres via morphology conserved thermal decomposition of MnCO 3 microspheres. Mater. Lett. 136, 85–89.

Rani, B.J., Ravina, M., Ravi, G., Ravichandran, S., Ganesh, V., Yuvakkumar, R., 2018. Synthesis and characterization of hausmannite (Mn 3 O 4) nanostructures. Surf. Interf. 11, 28–36.

Ristić, M., Musić, S., Popović, S., Dragčević, Đ., Marciuš, M., Ivanda, M., 2013. Synthesis and long-term phase stability of Mn3O4 nanoparticles. J. Mol. Struct. 1044, 255–261.

Rohani Bastami, T., Entezari, M.H., 2012. A novel approach for the synthesis of superparamagnetic Mn3O4 nanocrystals by ultrasonic bath. Ultrason. Sonochem. 19, 560–569.

Sahoo, R., Naik, P., Das, S., 2001. Leaching of manganese from low-grade manganese ore using oxalic acid as reductant in sulphuric acid solution. Hydrometallurgy 62, 157–163.

Selvan, R.K., Perelshtein, I., Perkas, N., Gedanken, A., 2008. Synthesis of hexagonal-shaped SnO2 nanocrystals and SnO2@ C nanocomposites for electrochemical redox supercapacitors. J. Phys. Chem. C 112, 1825–1830.

Shaik, D.P., Pitcheri, R., Qiu, Y., Hussain, O., 2019. Hydrothermally synthesized porous Mn3O4 nanoparticles with enhanced electrochemical performance for supercapacitors. Ceram. Int. 45, 2226–2233.

Shao, Y., Ren, B., Jiang, H., Zhou, B., Lv, L., Ren, J., Dong, L., Li, J., Liu, Z., 2017. Dual-porosity Mn2O3 cubes for highly efficient dye adsorption. J. Hazard. Mater. 333, 222–231.

Sherin, J., Thomas, J., Suthagar, J., 2014. Combustion synthesis and magnetic studies of hausmannite, Mn3O4, nanoparticles. Int. J. Eng. Res. Dev. 10, 34–41.

Sinha, M.K., Purcell, W., 2019. Reducing agents in the leaching of manganese ores: a comprehensive review. Hydrometallurgy 187, 168–186.

Song, R., Feng, S., Wang, H., Hou, C., 2013. Effect of organic solvents on particle size of Mn3O4 nanoparticles synthesized by a solvothermal method. J. Solid State Chem. 202, 57–60.

Sun, W.-y., Su, S.-j., Wang, Q.-y., Ding, S.-l., 2013. Lab-scale circulation process of electrolytic manganese production with low-grade pyrolusite leaching by SO2. Hydrometallurgy 133, 118–125.

Tebble, R.S., Craik, D.J., 1969. Magnetic Materials.

Ullah, A.K.M.A., Kibria, A.K.M.F., Akter, M., Khan, M.N.I., Maksud, M.A., Jahan, R.A., Firoz, S.H., 2017. Synthesis of Mn 3 O 4 nanoparticles via a facile gel formation route and study of their phase and structural transformation with distinct surface morphology upon heat treatment. J. Saudi Chem. Soc. 21, 830–836.

Vazquez-Olmos, A., Redon, R., Rodriguez-Gattorno, G., Esther Mata-Zamora, M., Morales-Leal, F., Fernandez-Osorio, A.L., Saniger, J.M., 2005. One-step synthesis of Mn3O4 nanoparticles: structural and magnetic study. J. Colloid Interface Sci. 291, 175–180.

Wang, Y., Shao, X., Xu, H., Xie, M., Deng, S., Wang, H., Liu, J., Yan, H., 2013a. Facile Synthesis of Porous LiMn2O4 Spheres as Cathode Materials for High-power Lithium Ion Batteries, 226, pp. 140–148.

Wang, L., Chen, L., Li, Y., Ji, H., Yang, G., 2013b. Preparation of Mn3O4 nanoparticles at room condition for supercapacitor application. Powder Technol. 235, 76–81.

Wang, Y., Jin, S., Lv, Y., Zhang, Y., Su, H., 2017. Hydrometallurgical process and kinetics of leaching manganese from semi-oxidized manganese ores with sucrose. Minerals 7, 27.

Xiong, S., Li, X., Liu, P., Hao, S., Hao, F., Yin, Z., Liu, J., 2018. Recovery of manganese from low-grade pyrolusite ore by reductively acid leaching process using lignin as a low cost reductant. Miner. Eng. 125, 126–132.

Yusoff, N.F.M., Idris, N.H., Din, M.F.M., Majid, S.R., Harun, N.A., Rahman, M.M., 2020. Investigation on the electrochemical performances of Mn2O3 as a potential anode for Na-ion batteries. Sci. Rep. 10, 9207.

Zawrah, M., El Fadaly, E.A., Khattab, R., Aly, M., El Shafei, H., 2020. Synthesis and characterization of nano Mn3O4 and LiMn2O4 spinel from manganese ore and pure materials. Ceram. Int. 46, 17514–17522.

Zhang, J., Yuping, D., Shuqing, L., Xiaogang, L., Shunhua, L., 2010a. The effects of high magnetic field on the morphology and microwave electromagnetic properties of MnO2 powder. J. Solid State Chem. 183, 1490–1495.

Zhang, W., Cheng, C.Y., Pranolo, Y.J.H., 2010b. Investigation of Methods for Removal and Recovery of Manganese in Hydrometallurgical Processes, 101, pp. 58–63.

Zhang, X., Yu, P., Zhang, D., Zhang, H., Sun, X., Ma, Y., 2013. Room temperature synthesis of Mn3O4 nanoparticles: characterization, electrochemical properties and hydrothermal transformation to γ-MnO2 nanorods. Mater. Lett. 92, 401–404.